

Deep-learning based automatic segmentation of vesicles in cryo-electron tomograms

This manuscript ([permalink](#)) was automatically generated from [aseedb/deep-prepyto-paper@d0aec6f](#) on June 14, 2023.

Authors

- **Amin Khosrozadeh**

 [XXXX-XXXX-XXXX-XXXX](#) ·  [ameen-khosrowzadeh](#)

Institute of Anatomy, University of Bern, Bern, Switzerland; Graduate School for Cellular and Biomedical Sciences, University of Bern · Funded by Grant XXXXXXXX

- **Raphaella Seeger**

 [XXXX-XXXX-XXXX-XXXX](#) ·  [elatella](#)

Institute of Anatomy, University of Bern, Bern, Switzerland; Graduate School for Cellular and Biomedical Sciences, University of Bern

- **Julika Radecke**

 [0000-0002-5815-5537](#) ·  [julikaradecke](#)

Institute of Anatomy, University of Bern, Bern, Switzerland; Department of Neuroscience, Faculty of Health and Medical Science, 2200 Copenhagen N, University of Copenhagen, Copenhagen, Denmark; Diamond Light Source Ltd, Didcot, Oxfordshire, United Kingdom

- **Guillaume Witz**

 [0000-0003-1562-4265](#) ·  [guiwitz](#)

Science IT Service, University of Bern, Bern, Switzerland; Microscopy Imaging Center, University of Bern, Bern, Switzerland

- **Jakob B. Sørensen**

 [0000-0001-5465-3769](#) ·  [JBSorensen](#)

Department of Neuroscience, University of Copenhagen, Blegdamsvej 3B, 2200 Copenhagen N, Denmark · Funded by Novo Nordisk Fonden, NNF17OC0028516.; Carlsbergfondet, CF17-0875; Independent Research Fond Denmark, 8020-00228A; Lundbeckfonden, R277-2018-802

- **Benoît Zuber**

 [0000-0001-7725-5579](#) ·  [aseedb](#)

Institute of Anatomy, University of Bern, Bern, Switzerland · Funded by Swiss National Science Foundation, 179520; ERA-NET NEURON, NEURON-119

✉ — Correspondence possible via [GitHub Issues](#)

Abstract

Cryo-electron Tomography (Cryo-ET) has the potential to reveal cell structure down to atomic resolution. Nevertheless, cellular cryo-ET data is often highly complex and visualization, as well as quantification, of subcellular structures require image segmentation. Due to a relatively high level of noise and to anisotropic resolution in cryo-ET data, automatic segmentation based on classical computer vision approaches usually does not perform satisfyingly. For this reason, cryo-ET researchers have mostly performed manual segmentation.

Communication between neurons rely on neurotransmitter-filled synaptic vesicle (SV) exocytosis. Recruitment of SVs to the plasma membrane is an important means of regulating exocytosis and is influenced by interactions between SVs. Cryo-ET study of the spatial organization of SVs and of their interconnections allows a better understanding of the mechanisms of exocytosis regulation. Extremely accurate SV segmentation is a prerequisite to obtain a faithful representation of SV state of connectivity. Hundreds to thousands of SVs are present in a typical synapse, and their manual segmentation is a time-consuming exercise, which has been recognized as a bottleneck by the community.

Several attempts to automate vesicle segmentation by classical computer vision or machine learning algorithms have not yielded very robust results. We addressed this problem by designing a workflow consisting of a U-Net convolutional network followed by post-processing steps. This combination yields highly accurate results. Furthermore, we provide an interactive tool for accurately segmenting spherical vesicles in a fraction of the time required by available manual segmentation methods. This tool can be used to segment vesicles that were missed by the fully automatic procedure or to quickly segment a handful of vesicles, while bypassing the fully automatic procedure. Our pipeline can in principle be used to segment any spherical vesicle in any cell type as well as extracellular vesicles.

Introduction

The fine architecture of cells can be investigated by cryo-electron tomography (cryo-ET) [1]. Cellular structures are preserved down to the atomic scale through vitrification and observation of the samples in a fully hydrated state. When a macromolecule is present in a sufficient number of copies in the cells imaged by cryo-ET, it is possible to obtain its atomic structure in situ using subtomogram averaging [2,3]. Cellular cryo-ET datasets are usually extremely complex, making them difficult to analyze. This is aggravated by the sensitivity of biological samples to electron radiation, which limits the signal-to-noise ratio in cryo-ET datasets [4]. Tomographic reconstructions are generated from a series of images of the sample acquired at different viewing angles. The geometry of the samples prevents acquisition at certain angles, resulting in anisotropic spatial coverage. The resolution in the directions close to the axis of the electron beam incident on the untilted sample is strongly reduced. This effect, commonly referred to as the missing-wedge artifact, further complicates data analysis. In particular, organelles fully bounded by a membrane appear to have holes at their top and bottom (relative to the electron beam axis) [4].

The synapse is a specialized cellular contact at which information is transmitted from a neuron to another. The former neuron is called presynaptic and the latter is postsynaptic. In most cases, the signal is transmitted by the release of neurotransmitters into the intercellular space. Neurotransmitters are stored in SVs and are released following the fusion of an SV with the presynaptic plasma membrane. A synapse contains hundreds of SVs and their mobility and recruitability for neurotransmitter release depends on inter-vesicle interactions through so-called connector structures [5]. The characterization of these interactions can be performed automatically with the pyto package, which implements a hierarchical connectivity approach to segment connectors

[6]. For accurate connector segmentation, an accurate segmentation of SVs is prerequisite. To date, SV segmentation has been performed manually, but given the large number of SVs per dataset, it is an extremely time-consuming process. Typically, one person spends 3 to 8 working days to segment a single dataset. Attempts to perform this task automatically based on classical computer vision algorithms have not yielded sufficiently accurate performance [7]. To alleviate this situation, we decided to develop an approach based on deep learning.

Convolutional neural networks (CNN) have been successfully employed to segment cryo-ET data [8]. Although entirely satisfying for visualization purposes, this approach has not met the requirements of pyto. A recent publication described accurate SV segmentation of transmission electron microscopy images using CNN, but it is limited to 2-dimensional (2D) images of resin-embedded synapses [9]. In the first study, cryo-ET data are decomposed in individual 2D slices, which are handed as separate input to the CNN. The independent output 2D prediction images are reassembled in a 3-dimensional (3D) stack [8]. As discussed above, membranes oriented approximately parallel to the plane of the 2D tomographic images are not resolved. In the absence of contextual knowledge of the other 2D images, the CNN fails to segment these regions of the vesicles. Hence, spherical vesicles appear open, whereas we expect closed spherical objects. To overcome this limitation, we used a 3D U-Net CNN that takes 3D images as input [10]. Weigert et al. [11] implemented a U-Net for content-aware restoration (CARE) of 3D fluorescence microscopy datasets. They showed that it can restore information from anisotropic and very noisy datasets. We implemented a 3D U-Net based on CARE building blocks and trained it with manually segmented datasets. This method provided good accuracy and was only slightly affected by the missing wedge artifact. Nevertheless, it was not sufficient for our downstream pyto analysis. Hence, we developed a post-processing method, which transforms the segmented objects into spheres and refines their radius and center location. The procedure includes an outlier detection procedure. This lead to a substantial accuracy improvement, which is reflected in pyto performances comparable to those obtained after manual SV segmentation. We also introduce a semi-automatic method to quickly fix wrongly segmented or missed SVs.

Although our set of procedures was developed with the use case of SV segmentation in mind, it can be used to segment any other types of biological spherical vesicles, such as transport vesicles, secretory vesicles, endocytic vesicles, and extracellular vesicles.

Results

In view of the effort required for the manual segmentation of SVs, we decided to develop an automatic segmentation procedure. Since we had previously manually segmented a number of tomograms with the program IMOD, we could use these segmentations as the ground truth [12]. We trained a U-Net with a set of 9 segmented tomograms of rat synaptosomes (see Materials and Methods). The learning progress was tracked by calculating the Dice coefficient and the loss value after each training epoch (Figure 1). The Dice coefficient for the training set was initially ~0.25 and rose to over 0.9 after approximately 50 epochs, while for the validation set, it rose to 0.8. The loss for the training set went from 0.55 and to values below 0.05 after 50 epochs while for the validation set it went from 1 and to slightly below 0.3 after the initial 50 epochs and then rose slightly.

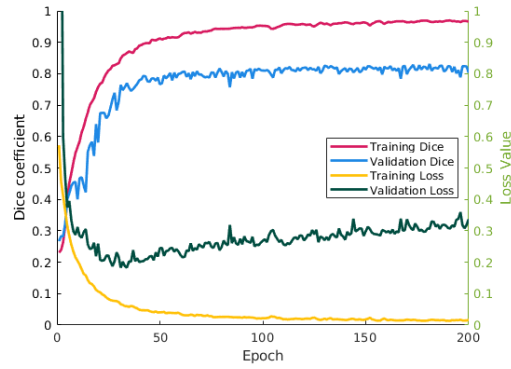


Figure 1: Dice coefficient and loss value for training and validation set.

We sought to further improve segmentation accuracy by feeding the probability mask output by the U-Net to a series of postprocess steps (Figure 2). Three sets of tomograms were used to assess the performances of the pipeline: 1) Training dataset : The 9 rat synaptosome tomograms that had been used for U-Net training, 2) Testing dataset: Another 9 rat synaptosome tomograms, 3) Testing dataset for generalizability: 12 mouse primary neuronal culture tomograms).

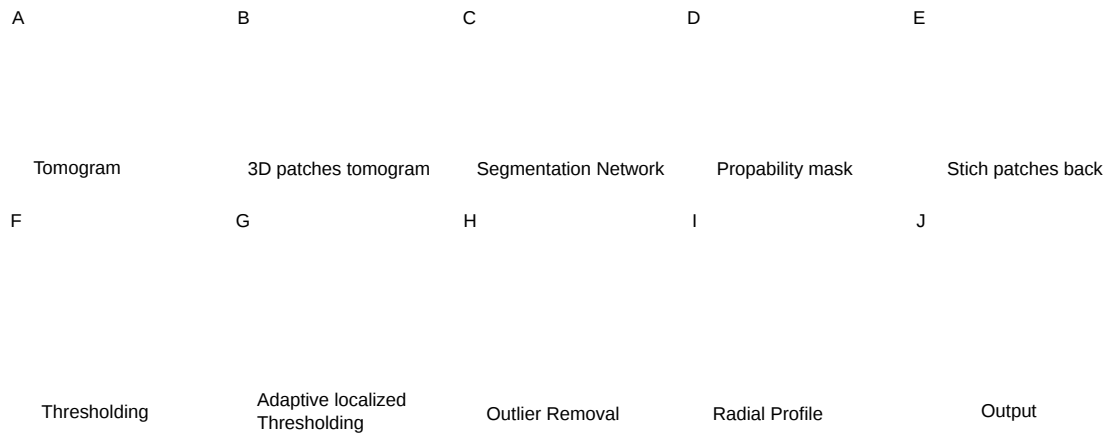


Figure 2: Pipeline of automatic segmentation. a) tomograms b) splitting in 3D patches c) Segmentation Network/ trained U-Net d) probability masks e) stitching patches back together f) thresholding g) adaptive localized thresholding h) outlier removal i) radial profile

Each tomogram was split into patches of 32^3 voxels. These patches were fed in the U-Net, which output a probability mask for those patches. To obtain a complete probability mask, the patches are stitched back together. The probability mask was binarized first with a global threshold value and then with an adaptive localized thresholding steps (Figure 2, Figure 3).

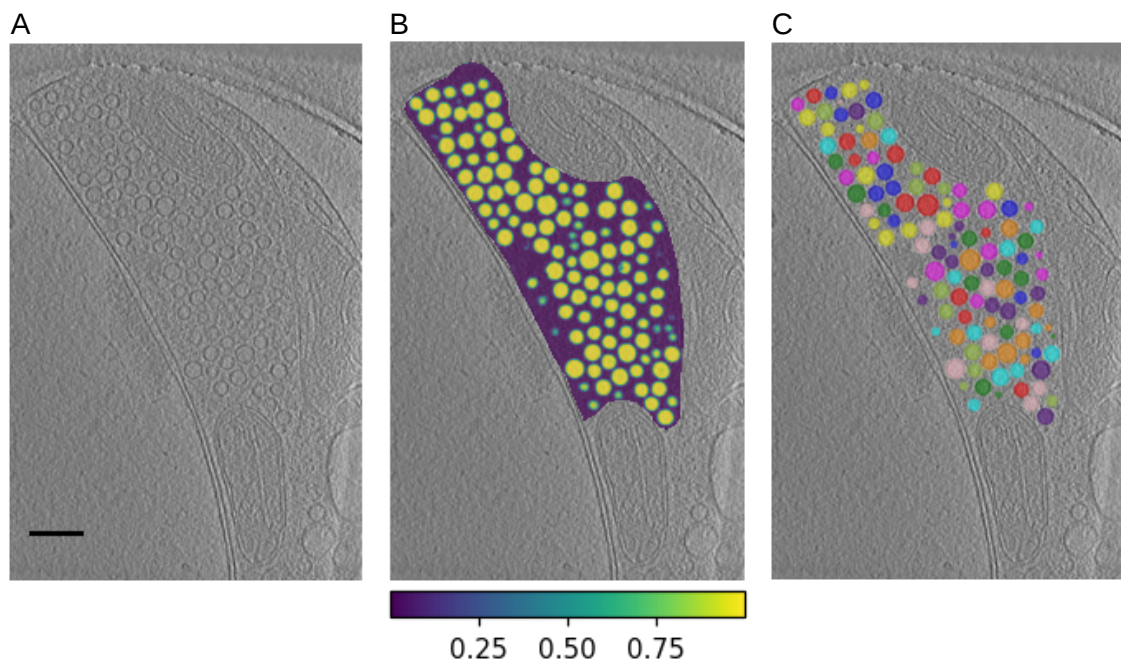


Figure 3: A 2D slice of an automatically segmented dataset. A) A section through a presynaptic terminal in a neuron tomogram. B) Predicted probability mask restricted to the segmentation region. Purple corresponds to a low SV probability and yellow to a high SV probability. C) Instance mask of the vesicles after post processing.

_more detail about global and adaptive localized threshold* For further optimization of the mask, outliers were removed. Removed outliers mostly consisted of vesicles which were only partially segmented, and vesicles which masks were adjacent due to proximity. The removed masks, which only partially traced the vesicles, were reevaluated by reducing or expanding their radius (Figure 4). _was the center of the vesicles also reevaluated?* _Its not clear or might be false sentence we didnt remove or re evaluate the mask?*

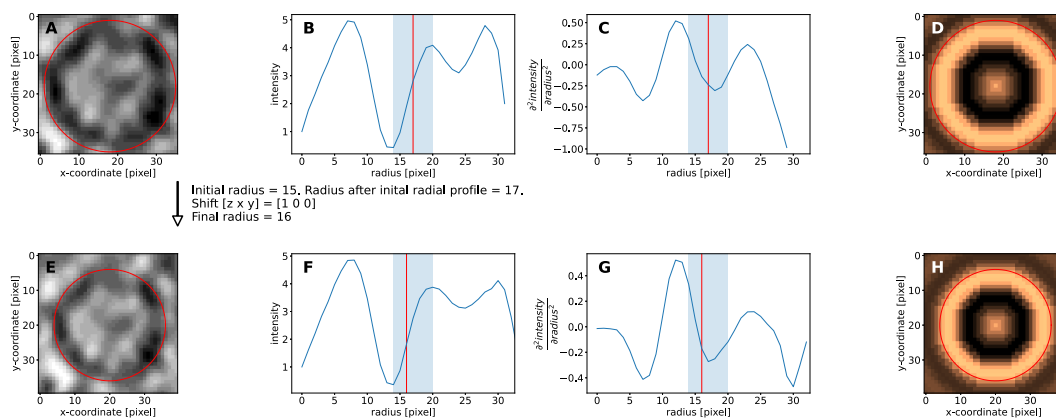


Figure 4: Vesicle radius and position through radial profile and cross-correlation Radial Profile Refinement A) couple of vesicles are not centered B) Radial Profile. Blue range is from membrane center to outer white halo center, this is the search range for the optimal radius. (smoothed by gaussian filtering) C) second derivative of radial profile E, F, H, G) Same as above columns after refinement

The adjacent vesicle masks were seperated (Figure _missing*). _how?*

_**missing Figure- Splitting adjacent vesicles. A) Examples of tomogram, no labels; B) raw label with connected vesicle-labels; C) modified label with seperated vesicles ---> for software: IMOD**

The Dice coefficient was used to track the global congruence between the manually segmented mask and the predicted mask within the different tomograms (Figure 5).

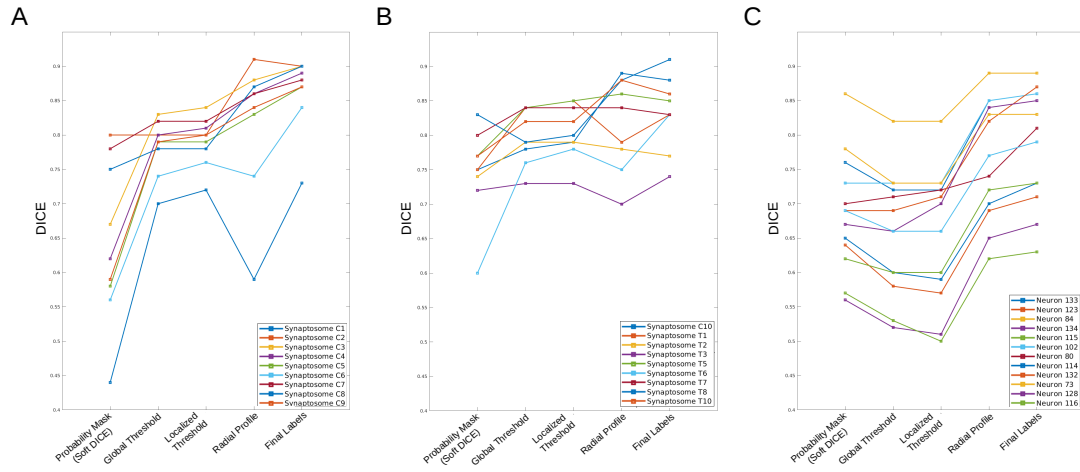


Figure 5: Dice development during post-processing Dice development at different post processing steps of initial predicted mask (different colors correspond to different tomograms): A) synaptosomal training datasets B) synaptosomal test datasets c) neuron test datasets

Table 1: Evaluation of the segmentation on the synaptosome train set. Mask Dice: Mask Dice coefficient for the predicted mask; Final Label Dice: Dice coefficient after post-processing; δd : diameter error on correctly detected vesicle; Δc : average error center (nm); Number of Vesicles: number of expected vesicles; TP: True Positive; FN: False Negative; FP: False Positive

<i>Dataset</i>	<i>Mask Dice</i>	<i>Final Label Dice</i>	δd	Δc (nm)	<i>Number of Vesicles</i>	<i>TP</i>	<i>FN</i>	<i>FP</i>
Synaptosome C1	0.44	0.73	0.07	2.55±1.56	223	198	26	49
Synaptosome C2	0.8	0.9	0.05	2.12±1.06	105	103	2	1
Synaptosome C3	0.67	0.9	0.05	1.86±1.24	128	127	1	6
Synaptosome C4	0.62	0.89	0.03	1.78±0.92	144	141	3	4
Synaptosome C5	0.58	0.87	0.04	1.86±1.00	214	209	5	13
Synaptosome C6	0.56	0.84	0.04	1.92±1.05	104	102	2	16
Synaptosome C7	0.78	0.88	0.06	1.86±0.90	184	184	0	16
Synaptosome C8	0.75	0.9	0.05	1.70±0.93	132	126	6	1
Synaptosome C9	0.59	0.87	0.05	1.87±0.91	135	132	3	14
Average	0.64±0.11	0.86±0.05	0.05	1.95±1.08	152.22	97.00%	3.00%	7.30%

Table 2: Evaluation of the segmentation on the synaptosome test set (same sample type as the train set). For the meaning of the columns, see Table 1.

<i>Dataset</i>	<i>Mask Dice</i>	<i>Final Label Dice</i>	δd	Δc (nm)	<i>Number of Vesicles</i>	<i>TP</i>	<i>FN</i>	<i>FP</i>
Synaptosome C10	0.75	0.88	0.07	1.86±1.18	129	123	6	5
Synaptosome T1	0.75	0.83	0.11	2.66±1.52	699	687	12	33

<i>Dataset</i>	<i>Mask Dice</i>	<i>Final Label Dice</i>	δd	$\Delta c (nm)$	<i>Number of Vesicles</i>	<i>TP</i>	<i>FN</i>	<i>FP</i>
Synaptosome T2	0.74	0.77	0.11	2.27±1.84	122	117	5	2
Synaptosome T3	0.72	0.74	0.11	3.64±2.22	434	397	37	57
Synaptosome T5	0.77	0.85	0.08	2.20±1.26	535	526	9	25
Synaptosome T6	0.6	0.83	0.07	2.02±1.12	373	353	20	42
Synaptosome T7	0.8	0.83	0.06	2.22±1.14	110	107	3	9
Synaptosome T8	0.83	0.91	0.04	2.09±1.04	100	99	1	2
Synaptosome T10	0.77	0.86	0.05	1.96±1.04	77	74	3	6
Average	0.75±0.06	0.83±0.05	0.08	2.32±1.43	286.56	96.30%	3.70%	6.10%

Table 3: Evaluation of the segmentation on the neuron test set (different sample type as the train set). For the meaning of the columns, see Table 1.

<i>Dataset</i>	<i>Mask Dice</i>	<i>Final Label Dice</i>	δd	$\Delta c (nm)$	<i>Number of Vesicles</i>	<i>TP</i>	<i>FN</i>	<i>FP</i>
Neuron 133	0.76	0.86	0.05	2.16±1.32	523	467	56	8
Neuron 123	0.64	0.71	0.05	2.05±1.18	66	58	8	2
Neuron 84	0.86	0.89	0.06	1.44±0.75	498	484	14	1
Neuron 134	0.56	0.67	0.09	2.87±2.50	638	384	254	63
Neuron 115	0.57	0.63	0.08	3.56±3.23	170	123	47	32
Neuron 102	0.73	0.86	0.05	1.47±0.79	103	86	17	1
Neuron 80	0.7	0.81	0.07	2.67±2.00	111	102	9	3
Neuron 114	0.65	0.73	0.07	2.68±1.79	131	93	38	9
Neuron 132	0.69	0.87	0.03	1.65±1.26	135	129	6	32
Neuron 73	0.78	0.83	0.06	2.93±2.00	526	483	43	2
Neuron 128	0.67	0.85	0.04	2.33±1.70	252	232	20	19
Neuron 116	0.62	0.73	0.07	2.38±1.82	296	207	89	35
Average	0.69±0.09	0.79±0.09	0.06	2.35±1.83	287.42	83.60%	16.40%	7.90%

Our method transfers well across datasets even without fine-tuning which shows robustness and generalization.

Comparison of manual segmentation with automatic deep-learning based segmentation

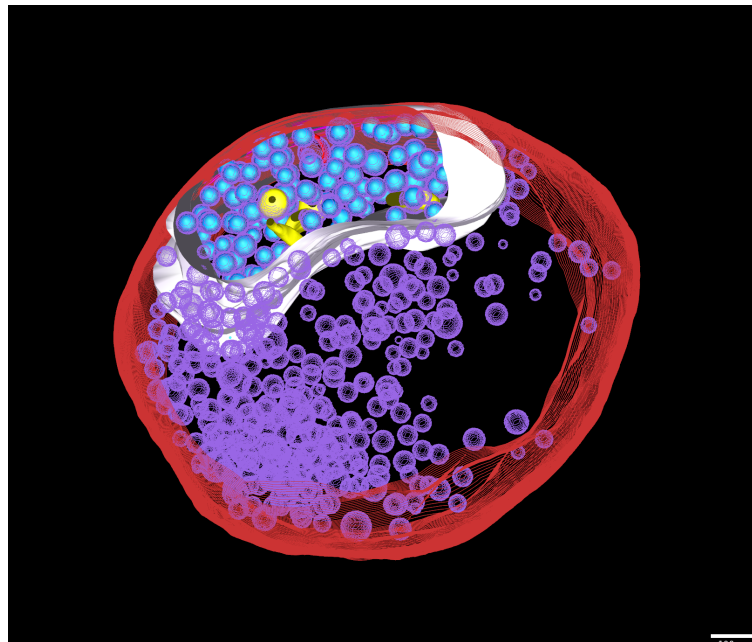


Figure 6: 3D model of manual segmented and automatically segmented synaptosome.

Discussion

While the Dice coefficient is a good global measure to assess the predictions in comparison to the ground truth, it is difficult to assess local segmentation accuracy. For example, a single generated vesicle label containing several close connected vesicles would not be practical for further analysis for the researcher although it could have almost the same dice value. What is important for actual usage of the software would be the number and percentage of true-detected vesicles, false-positive and false-negative rates.

Center error: If we measure each axis error it will reveal that human bias in segmentation is more affected on the Z-axis. [we didn't show it in number but its checked the hypothesis] `_we cannot claim something without showing it. ---> this would belong into results*`

3d unet good for 3D processing recent Nature methods paper by Ben Engel, DeepFinder -> Relion for STA creates mask to find more using dl -what are they doing, maybe compare that in the text, different aims; we might compare results we achieve (keep as bonus, revision)

Outlook

implement automatic cell-outline and active zone segmentation as deep learning workflow using UNet
implement automatic connector and tether segmentation as a deep learning workflow using UNet

Materials and methods

Cryo-electron Tomography Datasets

Two datasets of different origin were used as input and test subjects for the automatic segmentation pipeline, respectively. They consisted in rat synaptosomes primary neuron cultures derived from mice. The preparation procedure of the samples from which the datasets were obtained as well as the biological analysis of these datasets was previously reported [13].

Manual segmentation and automatic interboundary segment detection

Manual segmentation of SVs, mitochondria, the active zone PM, and of the segmentation region was done in IMOD (Figure S4A&B) [12]. SVs were segmented as spheres. The segmentation region marked the region to be analyzed by Pyto [6]. The analysis by Pyto was essentially the same as described previously [5,6]. In short, the segmented region is divided in 1 voxel thick layers parallel to the active zone for distance calculations. A hierarchical connectivity segmentation detects densities interconnecting boundaries. The boundaries were synaptic vesicles and the active zone PM. Detected intervesicular segments are termed connectors and segments connecting vesicles to the active zone PM are called tethers (Figure _add figure number*). Distance calculations respective to SVs were done from SV center. The segmentation procedure is conservative and tends to miss some tethers and connectors because of noise. Consequently, the numbers of tethers and connectors should not be considered as absolute values, but rather to compare experimental groups. As it was done before, an upper limit was set between 2100 and 3200 nm³ on segment volume. The tomograms that were used for this analysis were binned by a factor of 2 to 3, resulting in voxel sizes between 2.1 and 2.4 nm.

Pre-processing of manual segmentation outputs from IMOD for further use (jupyter notebook pre-pyto)

probably not necessary to mention output from IMOD to prepyto input label file procedure

put this somewhere else The used datasets included a total of 30 tomograms with heterogeneous pixel sizes, defocus and resolution.

1. 9 synaptosome datasets were used for training and validation.
2. 9 synaptosome datasets was used for test.
3. 12 Neuron dataset were used for assessing transfer learning potential.

Network architecture and training procedure

We used a U-Net with two downsampling stages and two convolutional layers per stages, with a kernel size of 3, and ReLU activation function based on the open-source CARE framework (Figure 7) [11]. Datasets were prepared by splitting the 3D tomographic volume of synaptosomes into 32³-voxel subvolumes and keeping only subvolumes occupied by a sufficient amount (> 1000 voxels) of binarized vesicle label. 860 subvolumes were used for training and 100 subvolumes were used for validation. We used the Adam optimizer on a binary cross-entropy loss function.

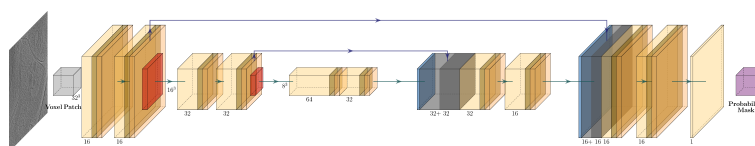


Figure 7: Network architecture used for vesicle segmentation. We used a U-Net based on the CARE framework [11]. The input is a cubic volume of 32³ voxels. The output is a per-pix probability cube of the same size as the input.

U-Net output threshold refinement

The probability mask output by the U-Net was first made binary by determining a global threshold value. To this end, the mask was binarized for a range of threshold values comprised between 0.8 and 1. For each probability value a 1-voxel thick label shell was computed. The shell mask was then applied on the input data and the average masked voxel intensity was computed. Since the shell of correctly segmented vesicles corresponds to the vesicle membrane, we expect low intensity pixels. The threshold value resulting in the minimal average intensity of the shell masked voxels was used as the global threshold.

Amin please write the equations for these steps. The probability mask was binarized using the global threshold and each separate segment was assigned an individual label with `scikit-image label` method.

A majority of vesicles were correctly segmented but we noticed some segments included two vesicles. We therefore evaluated each segment with two criteria based on the fact that synaptic vesicles have a homogenous size and are spherical. Firstly we calculated the volume z-score z for each segment:

$$z(S_i) = \frac{V(S_i) - \mu}{\sigma} \quad (1)$$

where S_i is the segment i , $V(S_i)$ is the volume of S_i , μ the average volume of all segments, and σ the standard deviation of the segment volumes. Secondly, we computed the segment extent e :

$$e(S_i) = \frac{V(S_i)}{B(S_i)} \quad (2)$$

where $B(S_i)$ is the volume of segment i bounding box. The extent of a sphere equals $\frac{\pi}{6}$. Segments with both a z-score $z > 1$ and an extent $e < 0.25$ were considered as potentially comprising two vesicles. For each of these segments, the probability mask threshold was increased until two distinct segments were generated. Subsequently, the extent and volume of all segments was evaluated again. Any segment with $e < 0.25$, or $e > 0.75$, or $V < k$ was discarded. This ensured that segments deviating highly from spherical shape and segments with a volume smaller than an acceptable volume k were removed.

Even if most synaptic vesicles were detected and well segmented, segmentation accuracy was not sufficient for our downstream application. To improve accuracy, each segment was converted to a spherical segment and its radius and position was refined. Initial spherical conversion was done by setting the center of the sphere C at the position of the centroid of the segment, while the radius r was defined as half the length of the bounding box longest edge. The segment position and radius was iteratively refined as follows. 1. The radial average $\langle I(d) \rangle$ was computed:

$$\langle I(d) \rangle = \frac{1}{4\pi^2 r^2} \int_0^{2\pi} \int_0^{2\pi} I(d, \theta, \phi) d\phi d\theta \quad (3)$$

where d is the radial distance from the segment center, θ the polar angle, and ϕ the azimuthal angle.

2. The radius of the vesicle r was updated as:

$$r = d_m + \frac{t_m}{2} \quad (4)$$

where d_m is the radial distance of center of the vesicle membrane, and t_m the thickness of the vesicle membrane. d_m was defined as the radial distance for which the radial average was minimal. $\frac{t_m}{2}$ was calculated as the distance between the center of the vesicle membrane and the minimum of the second derivative of the radial profile in the interval between the center of the vesicle membrane and the maximum of the Fresnel fringe outside the membrane. 3. The radial average was back projected

in 3-dimension:

$$I(x, y, z) = \langle I(\sqrt{x^2 + y^2 + z^2}) \rangle \quad (5)$$

where $(x, y, z) = (0, 0, 0)$ is the coordinate of the segment center. 4. We computed by cross-correlation the shift between the obtained 3-D average and the 3-D image in the cubic box with central coordinates C and edge length $l = 2r + c$, where c is a constant. C was updated by subtraction of the shift. 5. Steps 1 to 4 were repeated for a maximum of 10 iterations until convergence or until a total shift of $\frac{1}{2}\sqrt{3l_o^2}$, where l_o is the edge length of the initial box. The feature space of predicted vesicle labels was computed, containing membrane thickness t_m , membrane intensity ρ , and vesicle radius r . ρ was defined as the mean intensity of the radial average within the radial distance interval $[d_m - \frac{t_m}{2}, d_m + \frac{t_m}{2}]$.

Using this multivariate feature space, we detect outliers by computing Mahalanobis Distances (MD) on normalized variables using the covariance matrix of observation and obtaining The p-value of MD.

The sphere segments with a p-value higher than a defined threshold were discarded and the process was repeated iteratively. If the MD p-value of a specific vesicle was not in a specific margin range (0-10), their radial profile was recalculated, and the label entirely removed if they again failed to pass the margin of the p-value. Amin, please check what exactly was done with the outliers. And p-value cannot be higher than 1, while you wrote (0-10)

Analysis of Results

The evaluation framework was designed to assess the capabilities of the proposed toolbox for automatic synaptic vesicle segmentation. The framework was not only designed to evaluate quantitatively performance of the neural network, but rather assay the segmentation of vesicles in practice _unsure what the last part means*. _I tried to say we develop the software rather than an algorithm paper with ablation study kinda more tranfer learning but however for tranfer learning we might need add finetunning the network or say this sentence in other way*. The pipeline also generates a specific output format, which is necessary to further analyze the presynaptic tomograms via another pre-developed toolbox (Pyto), which segments small molecular filaments associated to the synaptic vesicles, titled tethers and connectors.

DICE

The _general form??* DICE coefficient for probabilistic subvolume maps was calculated after each epoch as a performance quantification while _during?* training. The probabilistic mask subvolumes were stitched back together, creating a probabilistic map of the whole tomogram. The Soft-DICE for the whole tomogram was calculated to evaluate the similarity of the predicted probability mask with ground truth. Note that soft-dice is equivalent to dice, when the input is binarized (which we will do at the end of the post-processing).

$$1 - \frac{2 \sum_{pixels} y_{true} y_{pred}}{\sum_{pixels} y_{true}^2 + \sum_{pixels} y_{pred}^2}$$

_shouldn't it be voxels instead of pixels??* _yes voxel is right*

THE DICE was also employed to monitor all stages of post-processing on the eventual label file, to observe the effect of each post-processing step.

Diameter Error

The diameter of a vesicle is one of its relevant characterizations, and it is predefined (see Outlier Removal). `_which diameters are we using in this evaluation as input, pre- or post-outlier removal?*` `_after! I meant from that perentesis that radius or dimater we assume as one charectiristic of vesicle we might can write it better`
* The error of diameter estimation of true-detected vesicle is defined as 1 minus the proportion of diameters

$$\delta d = 1 - \frac{\min(dSi, dGTi)}{\max(dSi, dGTi)} \quad (6)$$

where dGTi is the diameter of each true manual segmented vesicle, and dSi is the diameter of its estimation.

Center error

The center error is an euclidean distance of ground truth and corresponds to true predicted vesicles `_true pos or true neg*`. A vesicle was defined as a true-detected vesicle if the predicted center was located inside the hand-segmented vesicle and the other way around the center of prediction was located inside the predicted vesicle. `_isn't this a bit too general, shouldn't this be a tighter evaluation?*` `_we assume this as hard condition to be true postive we could define like some % liek 50% intersection but this condition is generally harder` This means the volume of intersection of the estimated vesicle with the distance of d to a ground truth vesicle with radius R is:

$$V = \frac{1}{12}\pi(4R + d)(2R - d)$$

Manuscript preparation

The manuscript was written with the open and collaborative scientific writing package Manubot [14]. The source code and data for this manuscript are available at https://github.com/aseedb/synaptic_tomo_ms.

References

1. **Towards Visual Proteomics at High Resolution**
Felix JB Bäuerlein, Wolfgang Baumeister
Journal of Molecular Biology (2021-10) <https://doi.org/gn9t3v>
DOI: [10.1016/j.jmb.2021.167187](https://doi.org/10.1016/j.jmb.2021.167187) · PMID: [34384780](https://pubmed.ncbi.nlm.nih.gov/34384780/)
2. **Exploring high-resolution cryo-ET and subtomogram averaging capabilities of contemporary DEDs**
Martin Obr, Wim JH Hagen, Robert A Dick, Lingbo Yu, Abhay Kotecha, Florian KM Schur
Cold Spring Harbor Laboratory (2022-01-10) <https://doi.org/gn92pd>
DOI: [10.1101/2022.01.10.475481](https://doi.org/10.1101/2022.01.10.475481)
3. **High-resolution in situ structure determination by cryo-electron tomography and subtomogram averaging using emClarity**
Tao Ni, Thomas Frosio, Luiza Mendonça, Yuewen Sheng, Daniel Clare, Benjamin A Himes, Peijun Zhang
Nature Protocols (2022-01-12) <https://doi.org/gn92pc>
DOI: [10.1038/s41596-021-00648-5](https://doi.org/10.1038/s41596-021-00648-5) · PMID: [35022621](https://pubmed.ncbi.nlm.nih.gov/35022621/) · PMCID: [PMC9251519](https://pubmed.ncbi.nlm.nih.gov/PMC9251519/)
4. **STRUCTURAL STUDIES BY ELECTRON TOMOGRAPHY: From Cells to Molecules**
Vladan Lučić, Friedrich Förster, Wolfgang Baumeister
Annual Review of Biochemistry (2005-06-01) <https://doi.org/cfd27f>
DOI: [10.1146/annurev.biochem.73.011303.074112](https://doi.org/10.1146/annurev.biochem.73.011303.074112) · PMID: [15952904](https://pubmed.ncbi.nlm.nih.gov/15952904/)
5. **Quantitative analysis of the native presynaptic cytomatrix by cryoelectron tomography**
Rubén Fernández-Busnadiego, Benoît Zuber, Ulrike Elisabeth Maurer, Marek Cyrklaff, Wolfgang Baumeister, Vladan Lučić
Journal of Cell Biology (2010-01-11) <https://doi.org/b9c26b>
DOI: [10.1083/jcb.200908082](https://doi.org/10.1083/jcb.200908082) · PMID: [20065095](https://pubmed.ncbi.nlm.nih.gov/20065095/) · PMCID: [PMC2812849](https://pubmed.ncbi.nlm.nih.gov/PMC2812849/)
6. **Hierarchical detection and analysis of macromolecular complexes in cryo-electron tomograms using Pyto software**
Vladan Lučić, Rubén Fernández-Busnadiego, Ulrike Laugks, Wolfgang Baumeister
Journal of Structural Biology (2016-12) <https://doi.org/f9d5t2>
DOI: [10.1016/j.jsb.2016.10.004](https://doi.org/10.1016/j.jsb.2016.10.004) · PMID: [27742578](https://pubmed.ncbi.nlm.nih.gov/27742578/)
7. **Robust membrane detection based on tensor voting for electron tomography**
Antonio Martinez-Sanchez, Inmaculada Garcia, Shoh Asano, Vladan Lucic, Jose-Jesus Fernandez
Journal of Structural Biology (2014-04) <https://doi.org/f5zkj8>
DOI: [10.1016/j.jsb.2014.02.015](https://doi.org/10.1016/j.jsb.2014.02.015) · PMID: [24625523](https://pubmed.ncbi.nlm.nih.gov/24625523/)
8. **Convolutional neural networks for automated annotation of cellular cryo-electron tomograms**
Muyuan Chen, Wei Dai, Stella Y Sun, Darius Jonasch, Cynthia Y He, Michael F Schmid, Wah Chiu, Steven J Ludtke
Nature Methods (2017-08-28) <https://doi.org/gkjpj62>
DOI: [10.1038/nmeth.4405](https://doi.org/10.1038/nmeth.4405) · PMID: [28846087](https://pubmed.ncbi.nlm.nih.gov/28846087/) · PMCID: [PMC5623144](https://pubmed.ncbi.nlm.nih.gov/PMC5623144/)
9. **Automated Detection and Localization of Synaptic Vesicles in Electron Microscopy Images**
Barbara Imbrosci, Dietmar Schmitz, Marta Orlando
eneuro (2022-01) <https://doi.org/gn9n8k>
DOI: [10.1523/eneuro.0400-20.2021](https://doi.org/10.1523/eneuro.0400-20.2021) · PMID: [34983830](https://pubmed.ncbi.nlm.nih.gov/34983830/) · PMCID: [PMC8805189](https://pubmed.ncbi.nlm.nih.gov/PMC8805189/)

10. **3D U-Net: Learning Dense Volumetric Segmentation from Sparse Annotation**
Özgün Çiçek, Ahmed Abdulkadir, Soeren S Lienkamp, Thomas Brox, Olaf Ronneberger
arXiv (2016-06-22) <https://arxiv.org/abs/1606.06650>
11. **Content-aware image restoration: pushing the limits of fluorescence microscopy**
Martin Weigert, Uwe Schmidt, Tobias Boothe, Andreas Müller, Alexandr Dibrov, Akanksha Jain, Benjamin Wilhelm, Deborah Schmidt, Coleman Broaddus, Siân Culley, ... Eugene W Myers
Nature Methods (2018-11-26) <https://doi.org/gfkkfd>
DOI: [10.1038/s41592-018-0216-7](https://doi.org/10.1038/s41592-018-0216-7) · PMID: [30478326](https://pubmed.ncbi.nlm.nih.gov/30478326/)
12. **Computer Visualization of Three-Dimensional Image Data Using IMOD**
James R Kremer, David N Mastronarde, JRichard McIntosh
Journal of Structural Biology (1996-01) <https://doi.org/d9nfzw>
DOI: [10.1006/jsbi.1996.0013](https://doi.org/10.1006/jsbi.1996.0013) · PMID: [8742726](https://pubmed.ncbi.nlm.nih.gov/8742726/)
13. **Morphofunctional changes at the active zone during synaptic vesicle exocytosis**
Julika Radecke, Raphaela Seeger, Anna Kádková, Ulrike Laugks, Amin Khosrozadeh, Kenneth N Goldie, Vladan Lučić, Jakob B Sørensen, Benoît Zuber
Cold Spring Harbor Laboratory (2022-03-07) <https://doi.org/gpm26v>
DOI: [10.1101/2022.03.07.483217](https://doi.org/10.1101/2022.03.07.483217)
14. **Open collaborative writing with Manubot**
Daniel S Himmelstein, Vincent Rubinetti, David R Slochower, Dongbo Hu, Venkat S Malladi, Casey S Greene, Anthony Gitter
PLOS Computational Biology (2019-06-24) <https://doi.org/c7np>
DOI: [10.1371/journal.pcbi.1007128](https://doi.org/10.1371/journal.pcbi.1007128) · PMID: [31233491](https://pubmed.ncbi.nlm.nih.gov/31233491/) · PMCID: [PMC6611653](https://pubmed.ncbi.nlm.nih.gov/PMC6611653/)